Bulletin of the Seismological Society of America, Vol. 104, No. 2, pp. 1020–1030, April 2014, doi: 10.1785/0120130313 (reprint)

Ⓔ

Short Note

The 2013 M_w 7.7 Balochistan Earthquake: Seismic Potential of an Accretionary Wedge

by R. Jolivet, Z. Duputel,* B. Riel, M. Simons, L. Rivera, S. E. Minson, H. Zhang, M. A. G. Aivazis, F. Ayoub, S. Leprince, S. Samsonov, M. Motagh,† and E. J. Fielding

Abstract Great earthquakes rarely occur within active accretionary prisms, despite the intense long-term deformation associated with the formation of these geologic structures. This paucity of earthquakes is often attributed to partitioning of deformation across multiple structures as well as aseismic deformation within and at the base of the prism (Davis *et al.*, 1983). We use teleseismic data and satellite optical and radar imaging of the 2013 M_w 7.7 earthquake that occurred on the southeastern edge of the Makran plate boundary zone to study this unexpected earthquake. We first compute a multiple point-source solution from *W*-phase waveforms to estimate fault geometry and rupture duration and timing. We then derive the distribution of subsurface fault slip from geodetic coseismic offsets. We sample for the slip posterior probability density function using a Bayesian approach, including a full description of the data covariance and accounting for errors in the elastic structure of the crust. The rupture nucleated on a subvertical segment, branching out of the Chaman fault system, and grew into a major earthquake along a 50° north-dipping thrust fault with significant along-strike curvature. Fault slip propagated at an average speed of 3.0 km/s for about 180 km and is concentrated in the top 10 km with no displacement on the underlying décollement. This earthquake does not exhibit significant slip deficit near the surface, nor is there significant segmentation of the rupture. We propose that complex interaction between the subduction accommodating the Arabia–Eurasia convergence to the south and the Ornach Nal fault plate boundary between India and Eurasia resulted in the significant strain gradient observed prior to this earthquake. Convergence in this region is accommodated both along the subduction megathrust and as internal deformation of the accretionary wedge.

Online Material: Figures showing waveform fits, focal mechanism, root mean square misfit, variation of the shear modulus, covariance functions, and model predictions.

Introduction

The Makran plate boundary is a wide deformation zone extending 400 km from south to north and 1000 km from east to west in southeastern Iran and southwestern Pakistan. The plate boundary accommodates northward subduction of the Arabia and Ormara plates under Eurasia at approximately 3 cm/yr (Fig. 1; Reilinger *et al.*, 2006). The resulting partially emerged accretionary wedge grows by partitioning of deformation across subparallel fold-and-thrust fault systems that sole into a flat décollement at approximately 10 km depth (Ellouz-Zimmermann *et al.*, 2007; Smith *et al.*, 2012). To the east, northward motion of India with respect to Eurasia at 3 cm/yr is accommodated across the Chaman fault system, a 1200 km long, left-lateral fault system extending south toward the subduction zone through the Ghazaband and Ornach Nal fault systems (Lawrence *et al.*, 1981; Ambraseys and Bilham, 2003; Ader *et al.*, 2012; Szeliga *et al.*, 2012). Despite this rapid relative plate motion, seismic activity in this region is low with only two significant historic earthquakes (Szeliga *et al.*, 2012). The largest instrumentally

*Now at Institut de Physique du Globe de Strasbourg, UdS and EOST/CNRS UMR 7516, France.

†Also at Department of Surveying and Geomatics Engineering, University of Tehran, Tehran, Iran.

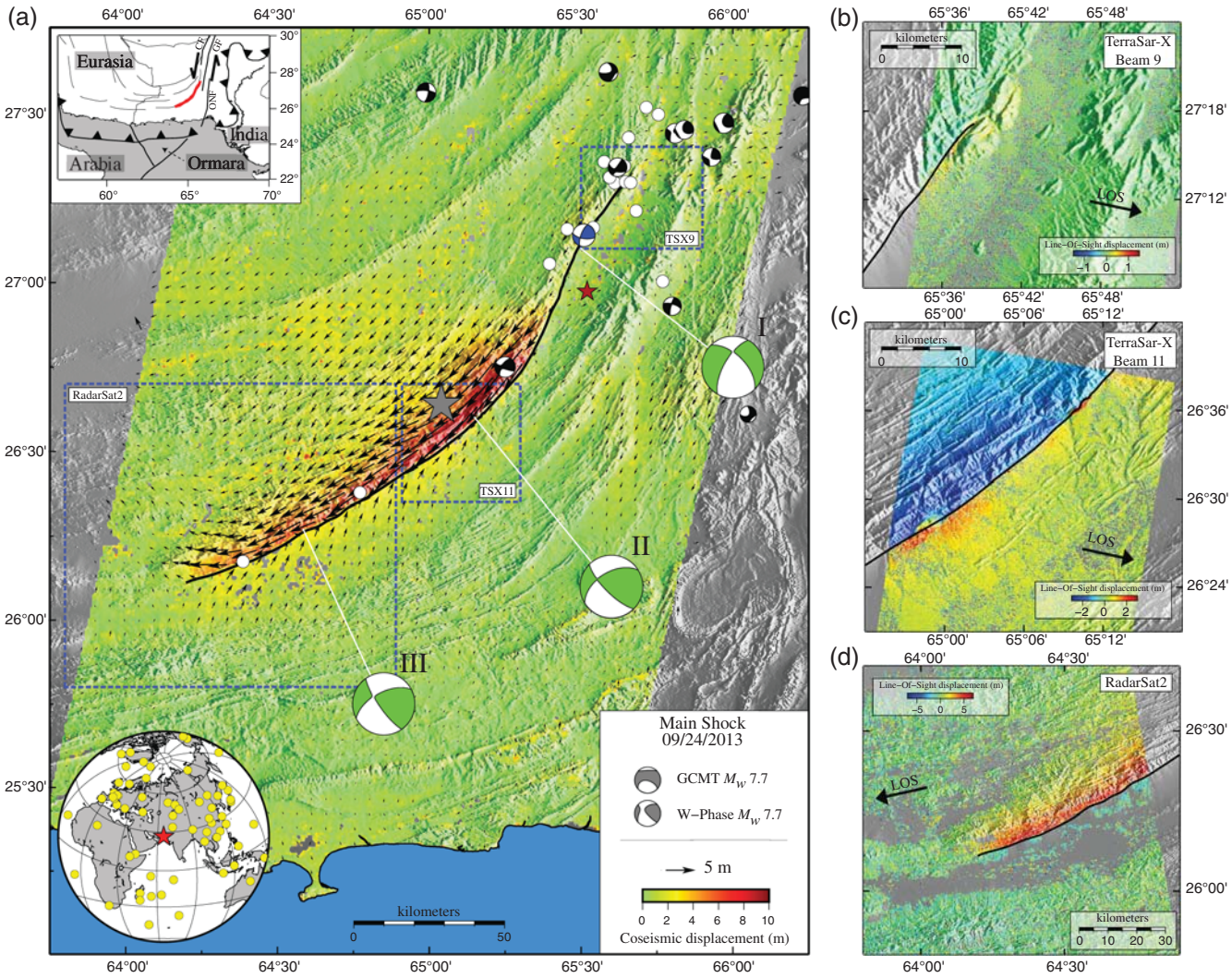

Figure 1. Surface displacements from optical image correlation and Line-of-Sight (LOS) range offsets map. (a) Map of surface displacements derived from correlation of pre- and post-earthquake Landsat 8 images (Avouac *et al.*, 2013). Black arrows indicate the displacement direction and amplitude averaged over a 3.5 km window. Green focal mechanisms correspond to the three sources solution derived from *W*-phase. The gray star indicates the Global Centroid Moment Tensor (Global CMT) centroid location. The dark red star indicates the United States Geological Survey epicenter location. Dark focal mechanisms correspond to $M_w \geq 5$ earthquakes prior to the mainshock (Global CMT). The blue focal mechanism is our body-wave solution of the largest aftershock (M_w 6.8). White circles are aftershocks from 24 September to 25 October 2013. Background shading is SRTM 90 m DEM (Farr and Kobrick, 2000). Dashed rectangles indicate areas covered by range offset maps (panels b, c, and d). Top left inset: Regional localization map (CF, Chaman fault; GF, Ghazaband fault; ONF, Ornach Nal fault). Bottom left inset: Global distribution of stations used for multiple source determination. (b) LOS range offset map for satellite TerraSAR-X (beam 9). (c) LOS range offset map for satellite TerraSAR-X (beam 11). (d) LOS range offset map for satellite RADARSAT-2. Continuous black line is the fault surface trace mapped from surface displacements shown on (a). Dark arrows indicate the direction from the ground to the satellite. Positive offsets are toward the satellite. As the RADARSAT-2 and TerraSAR-X line-of-sights point in nearly opposite directions, the difference in the sign change across the fault as seen in the two data sets implies that ground motion is predominantly horizontal.

recorded event is the 1945 M_w 8.1 Makran earthquake, which ruptured the subduction megathrust and generated a significant tsunami that washed the shores of Oman and India (Byrne *et al.*, 1992). Ten years earlier, in 1935, the M_w 7.5 Quetta earthquake occurred on the Ghazaband fault (Szeliga *et al.*, 2012). Although numerous smaller earthquakes with magnitude $M_w \leq 7$ have been documented, there are no reports of significant strike-slip earthquakes in at least the last 200 years along the Chaman fault system (Ambraseys and Bilham, 2003). On 24 September 2013, the M_w 7.7 Balochistan earthquake struck the Hoshab fault in the transition between the Chaman fault system and the accretionary wedge (Avouac *et al.*, 2013).

Global Positioning System (GPS) and Interferometric Synthetic Aperture Radar (InSAR) observations of the secular deformation between 2006 and 2012 suggest relatively shallow apparent locking depths (< 5 km) on several faults in the region (Szeliga *et al.*, 2012). Although the Ornach Nal fault accommodates approximately half of the 2.5–3 cm/yr of left-lateral motion between Eurasia and India, the remaining

1 cm/yr must be accommodated by a combination of aseismic fault slip, distributed deformation and possible future earthquakes (Szeliga *et al.*, 2012). Taken together, these observations were interpreted to suggest a low likelihood for large earthquakes in this region, making the 2013 event a surprise (Ambraseys and Bilham, 2003; Szeliga *et al.*, 2012).

The near real-time point-source focal mechanisms obtained for the 2013 M_w 7.7 Balochistan earthquake indicate oblique strike-slip faulting (Fig. 1). Such large strike-slip fault motion on a dipping structure is unprecedented. Additionally, different earthquake focal mechanisms, including *W*-phase, surface-wave, and body-wave solutions (U.S. Geological Survey), reveal a significant variation in the non-double-couple component. The largest aftershock, a strike-slip M_w 6.8 event on September 28 that is thought to have ruptured the same fault, has a purely double-couple mechanism (Fig. 1 and Ⓔ Fig. S1, available in the electronic supplement to this article). The non-double-couple components of point-source mechanisms for the principal event suggest significant source complexity, including a nonplanar fault geometry and/or a spatially complex distribution of fault slip.

Surface Displacement Derived from Optical and Synthetic Aperture Radar (SAR) Satellite Images

The 2013 Balochistan earthquake lies in a remote region of Pakistan. As a consequence, there is no existing permanent local geodetic network, and only a few campaign GPS sites are available on both sides of the rupture (Szeliga *et al.*, 2012). Thus, we rely on remote sensing techniques to image the surface deformation field. We use the east–west and north–south coseismic displacement field derived from correlation of optical images from the Landsat 8 satellite (Fig. 1; Avouac *et al.*, 2013). Surface displacements reveal a 180 km long rupture reaching the surface, allowing us to define the primary fault trace. As shown on Figure 2, maximum horizontal surface displacements are mostly in the fault-parallel direction and reach 10 m along the central section (26°35′ N) where both the Global Centroid Moment Tensor (Global CMT) and *W*-phase centroids are located, whereas to the north, surface fault slip is limited (< 1 m). The deformation field is spatially concentrated near the fault, suggesting fault slip occurs predominantly at shallow depths in agreement with the various estimates of centroid depths (< 15 km deep). The deformation pattern shows strong asymmetry across the fault with the degree of asymmetry varying along strike (Fig. 2). To the north, fault-parallel displacement profiles are symmetric across the fault, suggesting a subvertical source, whereas strongly asymmetric profiles are visible to the south, suggesting significant dip angle to the north.

Given the nonvertical fault dip, the geologic setting, and the moment tensors, we expect some portion of the fault may have slipped with a nonhorizontal rake. Thus, data providing constraints on the vertical coseismic displacements are crucial. We use range offset measurements derived from pre- and post-earthquake SAR acquisitions by the RADARSAT-2 (C-band) and TerraSAR-X (X-band) satellites (Fig. 1). RADARSAT-2 images were acquired on 31 October 2012 and 2 October 2013. Two sets of TerraSAR-X images were acquired on track 121 with two different beams on the same post-earthquake date, 27 September 2013. Pre-earthquake images on the northernmost beam 9 and beam 11 were acquired on 13 April 2009 and 22 March 2009, respectively. Because of the amplitude of the coseismic displacements and the low strain rate estimates in the area, the majority of the signal results from the earthquake.

We use the ROI_PAC software package to perform pixel offset tracking directly on the single-look complex TerraSAR-X images and correct the line-of-sight range offsets for topographic and orbital baseline effects (Rosen *et al.*, 2000). The final range pixel size is 1 m for both beams. We use the Gamma software to generate the line-of-sight range offsets from the RADARSAT-2 single-look complex (Wegmuller and Werner, 1997). The original pixel size is 12 m and 6 m in range and azimuth directions, respectively. Both range offset fields from TerraSAR-X and RADARSAT-2 are geocoded onto the SRTM 90 m digital elevation model (Farr and Kobrick, 2000).

TerraSAR-X range offsets confirm the low amplitude of the displacements to the north (Fig. 1). The fine resolution of the TerraSAR-X images (1 m) permit greater spatial resolution along strike, revealing local complexities in the deformation field. Two push-up structures can be identified at latitudes 26°27′ and 26°36′ along strike and correspond to local stepovers in the surface fault trace, suggesting segmentation of the fault on a 10 km scale.

W-Phase Moment Tensor and Multiple Sources Exploration

We compute a single-event point-source moment tensor inversion of global low frequency (1.67–5 mHz) *W*-phase waveforms (Kanamori and Rivera, 2008; Duputel *et al.*, 2012a; Fig. 1 and Ⓔ Fig. S2, available in the electronic supplement). We manually selected 139 well-distributed long-period *W*-phase traces within an epicentral distance of 90° filtered at long period using the 200–600 s passband. We obtain a moment magnitude M_w of 7.73. The mechanism is presented in Figures 1 and 3. To test the stability of this solution, we performed point-source inversions in multiple frequency bands (Ⓔ Fig. S3, available in the electronic supplement).

Although this solution fits the *W*-phase signals adequately at long period, the fundamental mode surface waves that follow are poorly predicted. As surface displacements suggest variable dip angle along strike, we explore an alternative solution based on three equally spaced point sources and simultaneously invert for the subevent time delays and double-couple parameters (Duputel *et al.*, 2012b; Fig. 1). This method is based on a modified version of the neighborhood algorithm sampler and has been already successfully applied to several complex earthquakes (Sambridge, 1999; Duputel *et al.*, 2012b). In this application,

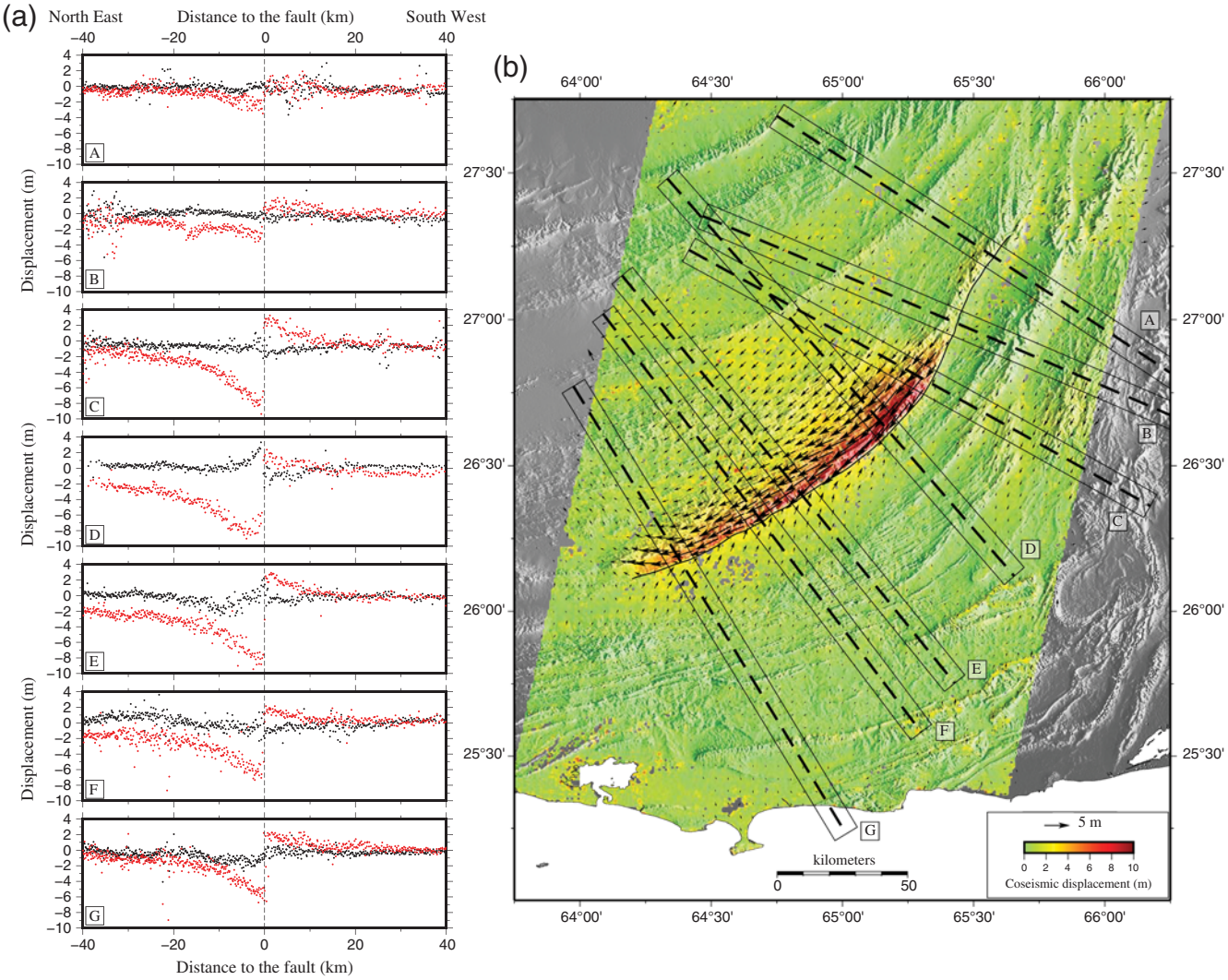

Figure 2. Asymmetry of the surface displacement field. (a) Fault-perpendicular profiles across the Hoshab fault of the displacement projected on the fault-parallel (red dots) and fault-perpendicular (dark dots) directions derived from the optical correlation of Landsat 8 images. Profile locations are indicated in (b) using letters A–G. To first order, profiles are asymmetric and show very low fault-normal displacement. (b) Map of surface displacements derived from correlation of pre- and post-earthquake Landsat 8 images.

the location of three point sources is fixed on the fault trace at 7.5 km depth. We invert for the strike, dip, rake, magnitude, and timing of each subevent. We use the *W*-phase waveforms from the stations shown on Figure 1 at shorter periods than is typically used for single-point-source inversions of M_w 7.5 earthquakes. The 90 selected traces filtered within the broadened passband 100–600 s yield the solution for three subevents presented in Figure 1. The centroid delays of sources I, II, and III are 10 s, 21 s, and 40 s with durations 10 s, 15 s, and 15 s, respectively. The magnitude of source II ($M_w \sim 7.5$) is larger than the two other subevents ($M_w \sim 7.3$). We used extensive neighborhood algorithm sampling of focal mechanism parameters to evaluate uncertainties. Based on the misfit of explored models, reasonable solutions can be found within 10% of relative increase in root mean square residual from the optimal model (Ⓔ Fig. S4, available in the electronic supplement).

Using three sources leads to a better fit to the *W*-phase waveforms in the broadened passband and significantly improves the reconstruction of late arrivals in the extended passband, not used in the inversion (Ⓔ Figs. S5–S9, available in the electronic supplement). Our three subevents solution reveals a clear rupture propagation from north to south with a total rupture duration of about 55 s and a corresponding average rupture velocity of 3.0 km/s (Fig. 1). The estimated focal mechanisms are in agreement with the varying strike of the fault trace and suggest a variation of the fault dip angle from a $70 \pm 10°$ north-dipping fault on the northern section to a $50 \pm 10°$ north-dipping fault in the southern section (Ⓔ Fig. S4, available in the electronic supplement). The dip angle along the northern section is confirmed by body-wave inversion of the M_w 6.8 aftershock of September 28, which favors a dip angle of ~70° (Ⓔ Fig. S1, available in the electronic supplement).

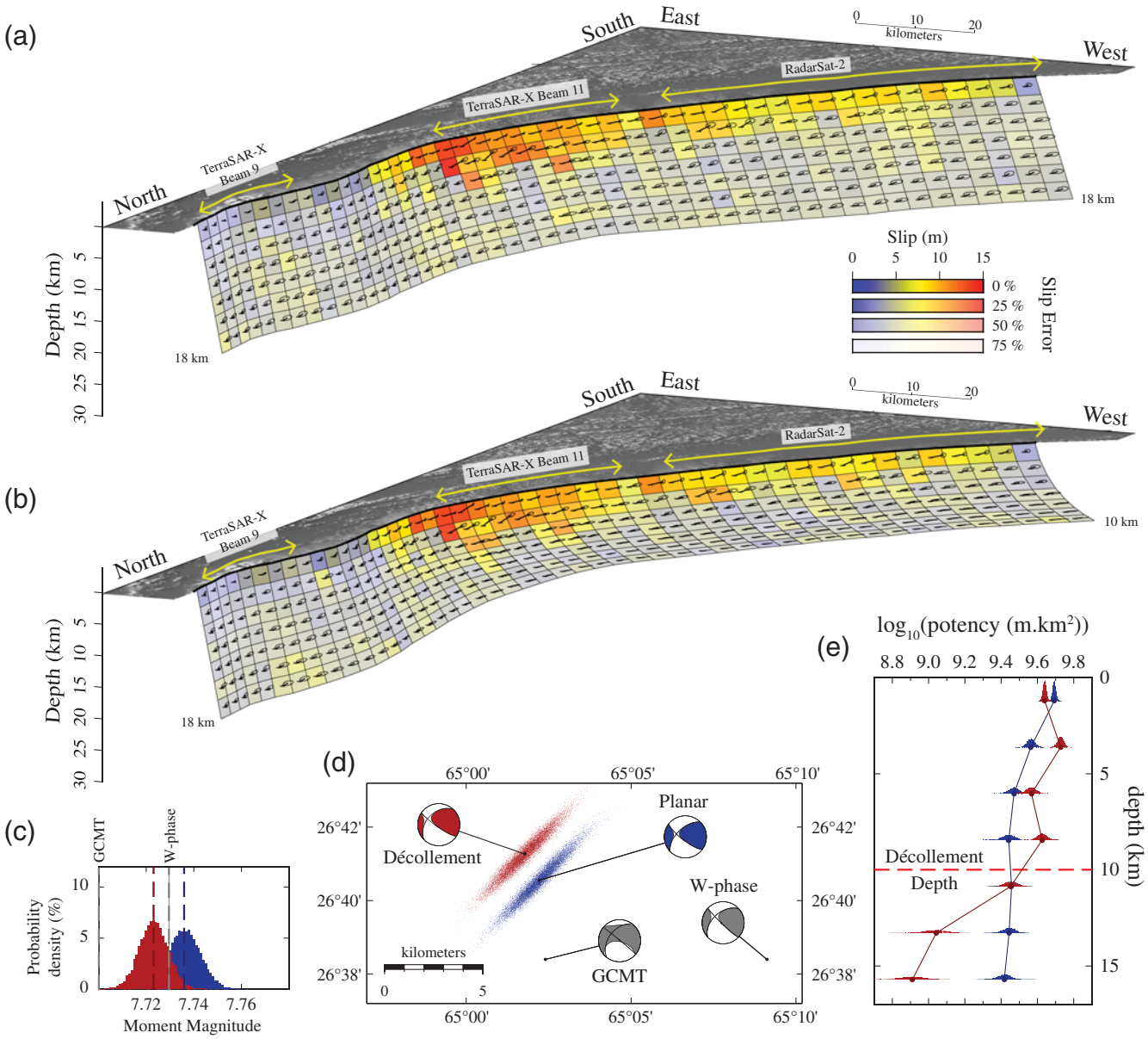

Figure 3. Preferred models and derived seismic quantities: (a) A 3D perspective view of the posterior mean coseismic slip models for the planar model and (b) for the listric model. The color of each subfault patch indicates the slip amplitude, whereas the brightness represents relative total slip uncertainty (i.e., the ratio of standard deviation and slip). Arrows and their associated 2σ error ellipse indicate the slip direction and uncertainty. Error ellipses are derived from the full posterior covariance, including correlation between strike-slip and dip-slip on each patch. Yellow arrows indicate the extent of the surface trace of the fault covered by the Synthetic Aperture Radar (SAR) range offset measurements. (c) Distribution of inferred magnitude for the planar fault model (blue) and listric fault model (red). Dashed gray lines indicate the Global CMT and *W*-phase magnitudes. (d) Equivalent point-source focal mechanisms and distributions of centroid locations for the planar (blue) and listric (red) slip models. Gray focal mechanisms are *W*-phase (this study) and Global CMT solutions. (e) Distribution of seismic potency as a function of depth for the planar fault model (blue) and listric fault model (red). The red dashed line indicates décollement depth. Note the potency decay at depth greater than 10 km for the listric fault model. Such depth variability results from the geometry we impose, as fewer patches are deeper than 10 km on the listric model.

A Fully Bayesian Inversion for the Final Slip Distribution

In this section, we describe in detail how careful handling of data and their associated uncertainties allows us to derive a realistic range of acceptable models fitting our observations. We average the range offset images over regularly spaced 2.5 km windows for RADARSAT-2 and 1.5 km for TerraSAR-X. We mask the push-up structure visible at latitude 26°27′ to avoid having to model this local complexity. We downsample the optical data set using a quad-tree algorithm based on the curvature of the displacement field (Simons *et al.*, 2002).

The surface trace of the fault tightly constrains the fault strike. We rely on the dip angle provided by the multiple point-source inversion to build a locally planar fault geometry, with constant dip along depth, between the surface and 18 km. However, structural investigation of the accretionary wedge suggests the presence of a décollement from which thrust faults splay upward at approximately 10 km depth (Ellouz-Zimmermann *et al.*, 2007). Whether such a structure could slip seismically has not been observed yet. We test such a hypothesis by building an alternative listric fault geometry with a depth-dependent dip angle ranging from the originally determined dips at the surface to a value of 10° at 10 km. Both fault models are made of 49×7 rectangular patches with dimensions of 5 km along strike and 3 km along dip.

To relate slip on individual subfault patches to surface displacement, we compute the Green's functions in a layered elastic half-space, following the elastic structure derived from surface waveform tomography (Zhu and Rivera, 2002; Maggi and Priestley, 2005; Ⓔ Fig. S10, available in the electronic supplement). On each fault patch, we solve for the along-strike and along-dip components of slip. Additional nuisance model parameters include a second-order polynomial function on the displacement maps from the correlation of optical images to account for long-wavelength artifacts and a linear function of range and azimuth on the SAR range offsets to account for possible orbital errors.

Our error model includes a data covariance modeling the correlation between observations as a function of distance (Lohman and Simons, 2005; Jolivet *et al.*, 2012) and a prediction error describing the uncertainties on the elastic properties in the medium (Duputel *et al.*, 2014). We use a two-step approach independently on each data set, optical and SAR, to build the data covariance matrix that reflects the measurement error. (1) We estimate the standard deviation over areas where deformation is negligible (0.47 m and 0.6 m for the east–west and north–south components of the optical data, respectively, 0.92 m for the RADARSAT-2 range offsets, and 0.45 m and 0.3 m for the TerraSAR-X range offsets on beam 11 and 9, respectively). (2) We build a covariance matrix assuming no correlations between data points, using the determined standard deviations, and perform a first inversion. (3) On the data residuals, we compute the empirical covariance function as a function of distance between observation points. (4) We then use the best-fit exponential function of the covariance function to build the full data covariance (Jolivet *et al.*, 2012; Ⓔ Figs. S11 and S12, available in the electronic supplement).

To account for prediction errors, we use a stochastic forward model based on a linearized formulation of the prediction uncertainty (Duputel *et al.*, 2012c). In contrast to a deterministic approach providing a single set of predictions for a given source model, our formulation produces a distribution of predictions for a given uncertainty in the shear modulus as a function of depth. Based on previous tomographic models of the region, we calculate the Green's functions for a reference 1D elastic structure and estimate the error on those Green's functions assuming 10%–40% uncertainty on the shear modulus, in agreement with the variability in available elastic models for this region (Ⓔ Fig. S10, available in the electronic supplement). The resulting prediction error introduces additional correlation between observations.

We use a Bayesian sampling approach to determine the *a posteriori* probability density function (hereafter PDF) of the slip distribution. Because of the high number of parameters involved (500+) and the limited number of observations, slip inversion problems are often nonunique and associated with large uncertainties. To cope with these fundamental limitations, we follow a Bayesian approach to derive the posterior PDF $p(\mathbf{m}|\mathbf{d}_{\text{obs}})$ describing the full ensemble of slip models $\mathbf{m}$ explaining our observations $\mathbf{d}_{\text{obs}}$. We use Cascading Adaptive Transitional Metropolis In Parallel (CATMIP), a Bayesian sampler, which combines the Metropolis algorithm with elements of simulated annealing and genetic algorithms to dynamically optimize the sampler's efficiency as it runs (Minson *et al.*, 2013). In order to sample our high-dimensional model space, we generate a large number of samples (100, 000+), therefore involving a large number of forward model evaluations. To do so, the CATMIP algorithm has been ported into a new framework (AlTar), which exploits the high efficiency of Graphic Processing Units, allowing a dramatic decrease in computing time. In the end, the algorithm transitions from the prior PDF $p(\mathbf{m})$ to the full posterior PDF of the model $\mathbf{m}$ by slowly increasing the information content in $\mathbf{d}$. We write

$$p(\mathbf{m}|\mathbf{d}_{\text{obs}}) \propto p(\mathbf{m}) \exp\left[-\frac{1}{2}(\mathbf{d}_{\text{obs}} - \mathbf{G}\mathbf{m})^T \mathbf{C}_\chi^{-1} (\mathbf{d}_{\text{obs}} - \mathbf{G}\mathbf{m})\right], \quad (1)$$

in which $\mathbf{m}$ is a vector of the model parameters, $\mathbf{d}_{\text{obs}}$ is the data, $\mathbf{G}$ is the matrix including the Green's functions, and $\mathbf{C}_\chi$ is the misfit covariance. The misfit covariance $\mathbf{C}_\chi$ combines the prediction uncertainty included in our stochastic forward model and the measurement errors. Data, predictions, and residuals are shown on Ⓔ Figures S13–S16, available in the electronic supplement.

Figure 3 shows the mean of the posterior PDF and the associated 2σ error for both tested models: the planar fault and the one including a décollement (hereafter called the listric fault). To first order, both models are similar, with one large region of dominantly strike-slip motion between the surface and 10 km depth and a maximum of slip of more than 10 m near the centroid derived from *W*-phase inversion. *A posteriori* uncertainties clearly indicate that slip is resolved in between the surface and 10 km depth (Fig. 3). In the northern section and at depths shallower than 10 km, slip is generally resolved to the 2σ confidence level.

In order to understand the impact of the different data types, we compared models constrained using just the optical imagery measurements of horizontal displacements with models that also included InSAR observations that provide a sensitivity to vertical displacements. In regions where InSAR data are available, we observe significantly lower uncertain-

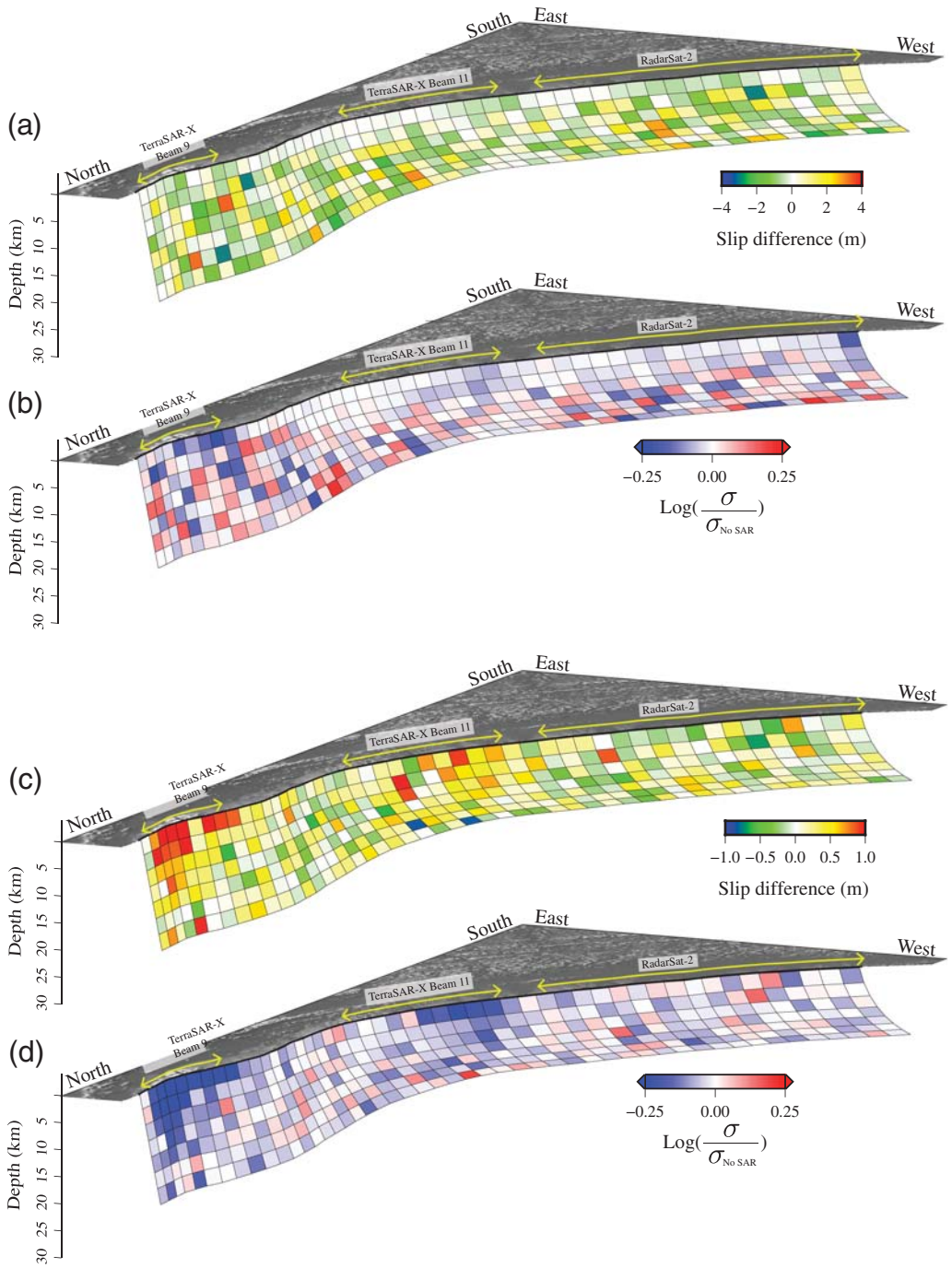

Figure 4. Comparison of the mean posterior model (MPM) with and without including the SAR range offset measurements. (a) and (c) Difference between the MPM of the obtained (a) strike-slip and (c) dip-slip component, including the SAR range offset measurements and the MPM without SAR range offsets. A positive sign means that not including SAR data leads to overestimated slip. (b) and (d) Logarithm of the ratio of the standard deviation of the (b) strike-slip and (d) dip-slip posterior distributions for the models obtained with and without including the SAR data. A negative value indicates that the estimates obtained including the SAR data has a smaller error than when these data are neglected. The range of values corresponds to factors of ±2 standard deviations.

ties (a factor of 2) on the inferred dip component of slip (Fig. 4). Such comparisons confirm the importance of acquiring observations sensitive to both horizontal and vertical displacements and raises our expectations for future radar satellite missions which should observe actively deforming regions from at least two viewing geometries.

Discussion and Conclusion

Although both models explain the data equally well, low-amplitude slip is observed at depths greater than 10 km if slip is allowed (i.e., on the planar fault model) and no slip is inferred on the flat section of the listric fault

model (Fig. 3 and Ⓔ Figs. S13–S17, available in the electronic supplement). Thus, we conclude that no significant slip occurred deeper than 10 km or along the décollement. In contrast to many other continental strike-slip earthquakes (Fialko *et al.*, 2005), slip potency is homogeneously distributed between the surface and a depth of 10 km on both models, suggesting no significant slip deficit at shallow depth (Fig. 3). Although spatially coherent residuals arise when comparing data to predictions from the listric model, the amplitude of such pattern (∼40 cm) does not exceed the noise level (50–70 cm), hence we cannot discriminate between models based on residuals. Still, the listric model is more consistent with a long-term geodynamical description of accretionary wedges, where fault slip occurs on thrust faults splaying up from a flat décollement with low apparent friction (Davis *et al.*, 1983; Dominguez *et al.*, 2003).

In order to compare our final slip distributions with the results from *W*-phase inversions, we estimate the equivalent moment tensor by summing moment tensors corresponding to slip on each subfault patch. We also determine the equivalent centroid position by averaging centers of patches weighted by the normalized scalar moment density (e.g., Dalhen and Tromp, 1998). The estimated centroid location is close to that determined by Global CMT and *W*-phase (Fig. 3). The posterior PDF of centroid locations for both models do not overlap, but the uncertainty on the *W*-phase location (±10 km) does not allow one to discriminate between models. The posterior moment magnitude follows a normal distribution, centered on 7.75 and 7.72 for the planar and listric models, respectively. Both models are compatible with the *W*-phase and Global CMT derived moment. Both models are within 12° from the *W*-phase moment tensor, whereas the difference with the Global CMT solution is slightly larger, about 14°–18° (Ⓔ Fig. S18, available in the electronic supplement).

Large intercontinental strike-slip ruptures often exhibit segmented ruptures, hence spatially complex slip distributions (Simons *et al.*, 2002; Çakir *et al.*, 2003; Hreinsdöttir *et al.*, 2003; Lasserre *et al.*, 2005). Fault segmentation has been mentioned as a key factor in earthquake nucleation, propagation, and arrest (Wesnousky, 2006). Here, slip is confined at shallow depth (i.e., between the surface and approximately 10 km depth), and its distribution is simple (i.e., we infer one single large region of slip). The long-wavelength along-strike curvature of the fault explains the non-double-couple component of teleseismic point-source mechanisms. The 10 km scale segmentation visible at the surface, as shown by the SAR range offset measurements, does not correspond to a significant segmentation of coseismic slip at depth. Still, the rupture initiated along a subvertical section of the fault and developed into a major earthquake on a more shallowly dipping section of the fault. The southward propagation stopped where the surface expression of the fault vanishes into a fold structure. We conclude that this rupture broke one single 150 km long curved segment after nucleating on a low-seismic-potential 30 km long subvertical segment and propagated without breaking through any obvious geometrical barrier. This earthquake may exemplify the role of fault geometry on the distribution of coseismic slip (e.g., Wesnousky, 2006; Klinger, 2010). We find no significant segmentation of the fault that would potentially impede rupture propagation. This lack of complexity appears to have resulted in a long and continuous rupture pattern.

The amplitude of slip along the northern section on average does not exceed 1–2 m and barely exceeds the posterior error estimates (Ⓔ Fig. S17, available in the electronic supplement). Despite the low slip in this section, this is the region where rupture initiated and that has experienced most of the aftershocks (Fig. 1). The subvertical dip angle suggests this section is the junction between the Chaman left-lateral fault system and the north-dipping thrust. Aseismic creep along the Chaman plate boundary has been invoked to account for the low historical rate of seismicity (Ambraseys and Bilham, 2003; Ul-Hadi *et al.*, 2013), with surface fault creep having been identified further north (Szeliga *et al.*, 2012). Observations and modeling of dynamic rupture suggest creeping segments and aseismic barriers as candidates for initiation of major ruptures (Lapusta and Liu, 2009; Bouchon *et al.*, 2011). Such a creeping segment, located north of the rupture, would explain the initiation of the rupture and why the rupture did not propagate northward, along a fault that has not ruptured in a significant earthquake for at least 200 years, despite the significant 1.5 cm/yr relative motion (Szeliga *et al.*, 2012).

In addition to possible occurrence of creep along this section of the Chaman fault system, a geometrical control may also be invoked to explain the observed southward propagation. The northern end of the Hoshab fault, north of the rupture, veers to a more north–south orientation. Here, left-lateral slip is partitioned between several parallel strands of the Chaman fault system, including the Ghazaband fault, on which occurred the 1935 M_w 7.5 Quetta earthquake and the Chaman fault itself (Lawrence *et al.*, 1981). Such geometrical complexity could have prevented a northward propagation (Wesnousky, 2006), leading to strain release on this segment through postseismic afterslip or distributed strain, hence the numerous aftershocks observed there.

At present, we do not have a complete quantitative understanding of the style and rates of strain accumulation in this region. Nor do we have a quantitative model for the accumulation of elastic strain on the Hoshab fault that led to the recent earthquake. The only available geodetically measured interseismic velocities in the area suggest that, in addition to slip on the Ornach Nal fault, 1 cm/yr of strike-slip motion must be accounted for in the direction parallel to the 2013 rupture trace, whereas 0.5 cm/yr of convergence builds up in the fault-normal direction (Fig. 5; Szeliga *et al.*, 2012). If the entire fault-parallel motion is accommodated by strike-slip motion on the Hoshab fault, approximately 500 years are required to buildup the slip produced in this earthquake. In this region, both the convergence between the Ormara plate and Eurasia and the strike-slip plate boundary with

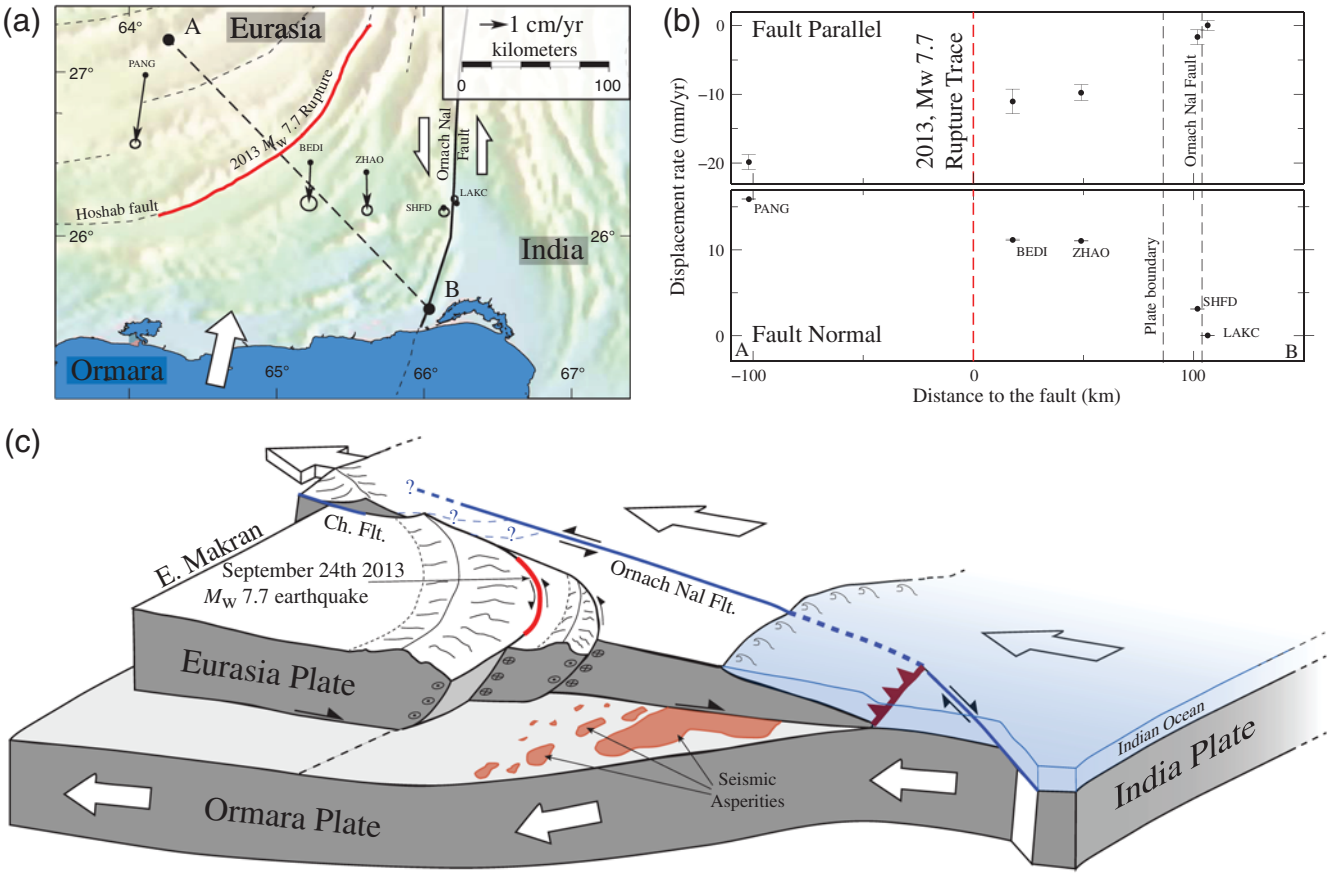

Figure 5. Assessing the interseismic strain budget. (a) Map of the southeastern Pakistani Makran, including the Ornach Nal fault (thick dark line) and the fault trace of the 2013 M_w 7.7 Balochistan earthquake. Arrows indicate interseismic velocities with their 1σ error ellipses from campaign measurements between 2006 and 2012 (Szeliga *et al.*, 2012). The dark dashed line indicates the profile onto which the data are projected in b. (b) GPS-derived interseismic velocities projected in the fault-parallel and the fault-perpendicular directions. Between sites BEDI and PANG, we observe an average displacement rate of 1 cm/yr in the fault-parallel direction and 0.5 cm/yr in the fault-normal direction. (c) Schematic block-diagram interpretation of ongoing deformation in the southeastern edge of the Makran accretionary wedge. Shortening is due to subduction of the Ormara plate, whereas shear motion is imposed by the northward motion of India. The wedge basal décollement is seismic in its up-dip portion, whereas it slips aseismically during the inter- and postseismic periods under the wedge, where seismic activity concentrates on faults that splay upward to the surface. (Ch. Flt: Chaman fault)

India are responsible for strain buildup inside the accretionary wedge. As slip during the 2013 earthquake is overwhelmingly left-lateral strike-slip, it presumably represents a portion of the 1 cm/yr missing between Eurasia and India. However, its orientation, oblique to the Ornach Nal plate boundary with a roughly 45° N strike, suggests a possible influence from strain accumulation along the Makran megathrust to the south (Fig. 5). Part of the corresponding convergence has to be accommodated within the prism to explain such rotation. We propose that the combination of shortening in the accretionary wedge, due to subduction of the Ormara plate, and the shear motion imposed by India resulted in the 2013 Balochistan earthquake (Fig. 5c).

Although geologic studies propose a fault model that incorporates a shallow dipping décollement (Ellouz-Zimmermann *et al.*, 2007), geodetic imaging data suggest negligible coseismic slip on this décollement, consistent with inferences in other similar geologic environments (Dominguez *et al.*, 2003; Avouac *et al.*, 2006). Our interpretation is that effective frictional properties do not allow for propagation of seismic ruptures onto the décollement and that this structure slips during the inter- and postseismic periods. The décollement may generate seismic ruptures of significant magnitude up-dip, as shown by the 1945 M_w 8.1 Makran earthquake, but it probably slips aseismically under the wedge (Fig. 5c), although one cannot exclude small seismic asperities might break occasionally (Satyabala *et al.*, 2012). Future analysis of postseismic deformation should illuminate the extent, amount, and direction of fault motion on the décollement thus helping to untangle the numerous ways in which the prism internal strain is accommodated between seismic and aseismic slip and distributed processes. The quantification of the partitioning of convergence between the subduction megathrust and internal deformation of the accretionary prism is essential in the assessment of seismic hazard both on megathrusts and within deforming forearcs of subduction zones.

Data and Resources

Early solutions for the Balochistan earthquake are from the United States Geological Survey website (http://earthquake.usgs.gov/earthquakes/eventpage/usb000jyiv; last accessed October 2013). The VarRes package for downsampling of optical and Synthetic Aperture Radar data can be downloaded from http://earthdef.caltech.edu (last accessed December 2013). RADARSAT-2 images are courtesy of MacDonald, Dettwiler, and Associates Ltd. and the Canadian Space Agency. TerraSAR-X data are courtesy of the German Aerospace Center, DLR.

Acknowledgments

Part of R. J. and L. R.'s funding were provided by the Tectonics Observatory. This research was supported by National Science Foundation (NSF) Grant EAR-1118239. This research was supported by the Southern California Earthquake Center (SCEC). SCEC is funded by NSF Cooperative Agreement EAR-0529922 and United States Geological Survey Cooperative Agreement 07HQAG0008. This is SCEC contribution 1899. This research was partly supported by the Gordon and Betty Moore Foundation. We thank the Canadian Space Agency for providing RADARSAT-2 data. TerraSAR-X original data are copyrighted by the German Aerospace Agency (DLR) and were provided under project Motagh-GEO1217. Part of this research was supported by the National Aeronautics and Space Administration Earth Surface and Interior focus area and performed by the Jet Propulsion Laboratory, California Institute of Technology. We thank J.-P. Avouac, J.-P. Ampuero, and H. Kanamori for their constructive comments and contributions. We thank the Associate Editor R. Bürgmann, R. Bilham (reviewer), and an anonymous reviewer for their constructive comments, which helped improve this manuscript.

References

Ader, T., J.-P. Avouac, J. Liu-Zeng, H. Lyon-Caen, L. Bollinger, J. Galetzka, J. Genrich, M. Thomas, K. Chanard, S. N. Sapkota, S. Rajaure, P. Shrestha, L. Ding, and M. Flouzat (2012). Convergence rate across the Nepal Himalaya and interseismic coupling on the main Himalayan thrust: Implications for seismic hazard, *J. Geophys. Res.* **117,** no. B4, B04403, doi: 10.1029/2011JB009071.

Ambraseys, N. N., and R. Bilham (2003). Earthquakes and associated deformation in northern Baluchistan 1892–2001, *Bull. Seismol. Soc. Am.* **93,** no. 4, 1573–1605.

Avouac, J.-P., F. Ayoub, S. Leprince, O. Konca, and D. V. Helmberger (2006). The 2005, M_w 7.6 Kashmir earthquake: Sub-pixel correlation of ASTER images and seismic waveforms analysis, *Earth Planet. Sci. Lett.* **249,** nos. 3/4, 514–528.

Avouac, J.-P., F. Ayoub, S. Wei, J.-P. Ampuero, L. Meng, S. Leprince, R. Jolivet, Z. Duputel, and D. Helmberger (2014). The 2013, M_w 7.7 Balochistan earthquake, energetic strike-slip reactivation of a thrust fault, *Earth Planet. Sci. Lett.* **391,** 128–134, doi: 10.1016/j.epsl.2014.01.036.

Bouchon, M., H. Karabulut, M. Aktar, S. Ozalaybey, J. Schmittbuhl, and M. P. Bouin (2011). Extended nucleation of the 1999 M_w 7.6 Izmit earthquake, *Science* **331,** no. 6019, 877–880.

Byrne, D. E., L. R. Sykes, and D. M. Davis (1992). Great thrust earthquakes and aseismic slip along the plate boundary of the Makran subduction zone, *J. Geophys. Res.* **97,** no. B1, 449–478.

Çakir, Z., J. B. de Chabalier, R. Armijo, R. Meyer, A. A. Barka, and G. Peltzer (2003). Coseismic and early post-seismic slip associated with the 1999 Izmit earthquake (Turkey), from SAR interferometryand tectonic field observations, *Geophys. J. Int.* **155,** 93–110.

Dalhen, F. A., and J. Tromp (1998). *Theoretical Global Seismology*, Princeton University Press, Princeton, New Jersey, 169 pp.

Davis, D. M., J. Suppe, and F. A. Dahlen (1983). Mechanics of fold-and-thrust belts and accretionary wedges, *J. Geophys. Res.* **88,** no. B2, 1153–1172.

Dominguez, S., J.-P. Avouac, and R. Michel (2003). Horizontal coseismic deformation of the 1999 Chi-Chi earthquake measured from SPOT satellite images: Implications for the seismic cycle along the western foothills of central Taiwan, *J. Geophys. Res.* **108,** no. B2, 2083.

Duputel, Z., P. S. Agram, M. Simons, and S. E. Minson (2014). Accounting for prediction error when inferring subsurface fault slip, *Geophys. J. Int.* doi: 10.1093/gji/ggt517.

Duputel, Z., H. Kanamori, V. C. Tsai, and L. Rivera (2012b). The 2012 Sumatra great earthquake sequence, *Earth Planet. Sci. Lett.* **351/352,** 247–257.

Duputel, Z., L. Rivera, Y. Fukahata, and H. Kanamori (2012c). Uncertainty estimations for seismic source inversions, *Geophys. J. Int.* **190,** no. 2, 1243–1256.

Duputel, Z., L. Rivera, H. Kanamori, and G. Hayes (2012a). *W* phase source inversion for moderate to large earthquakes (1990–2010), *Geophys. J. Int.* **189,** no. 2, 1125–1147.

Ellouz-Zimmermann, N., E. Deville, C. Müller, S. Lallemant, A. B. Subhani, and A. R. Tabreez (2007). Impact of sedimentation on convergent margin tectonics: Example of the Makran accretionary prism (Pakistan), in *Thrust Belts and Foreland Basins*, O. Lacombe, F. Lavé, F. M. Roure, and J. Verges (Editors), Springer, Berlin.

Farr, T. G., and M. Kobrick (2000). Shuttle radar topography mission produces a wealth of data, *Eos Trans. AGU* **81,** no. 48, 583–585.

Fialko, Y., D. Sandwell, M. Simons, and P. Rosen (2005). Three-dimensional deformation caused by the Bam, Iran, earthquake and the origin of shallow slip deficit, *Nature* **435,** no. 7040, 295–299.

Hreinsdöttir, S., J. T. Freymueller, H. J. Fletcher, C. F. Larsen, and R. Bürgmann (2003). Coseismic slip distribution of the 2002 M_w 7.9 Denali fault earthquake, Alaska, determined from GPS measurements, *Geophys. Res. Lett.* **30,** no. 13, 1670.

Jolivet, R., C. Lasserre, M. P. Doin, S. Guillaso, G. Peltzer, R. Dailu, J. Sun, Z. K. Shen, and X. Xu (2012). Shallow creep on the Haiyuan fault (Gansu, China) revealed by SAR interferometry, *J. Geophys. Res.* **117,** no. B6, doi: 10.1029/2011JB008732.

Kanamori, H., and L. Rivera (2008). Source inversion of *W* phase: Speeding up seismic tsunami warning, *Geophys. J. Int.* **175,** no. 1, 222–238.

Klinger, Y. (2010). Relation between continental strike-slip earthquake segmentation and thickness of the crust, *J. Geophys. Res.* **115,** no. B07306, doi: 10.1029/2009JB006550.

Lapusta, N., and Y. Liu (2009). Three-dimensional boundary integral modeling of spontaneous earthquake sequences and aseismic slip, *J. Geophys. Res.* **114,** no. B9, 10.1029/2008JB005934.

Lasserre, C., G. Peltzer, F. Crampé, Y. Klinger, J. Van der Woerd, and P. Tapponnier (2005). Coseismic deformation of the 2001 $M_w = 7.8$ Kokoxili earthquake in Tibet, measured by synthetic aperture radar interferometry, *J. Geophys. Res.* **110,** no. B12, doi: 10.1029/2004JB003500.

Lawrence, R. D., S. H. Khan, K. A. DeJong, A. Farah, and R. S. Yeats (1981). Thrust and strike slip fault interaction along the Chaman transform zone, Pakistan, *Geol. Soc. London* **9,** 363–370, doi: 10.1144/GSL.SP.1981.009.01.33.

Lohman, R. B., and M. Simons (2005). Some thoughts on the use of InSAR data to constrain models of surface deformation: Noise structure and data downsampling, *Geochem. Geophys. Geosys.* **6,** no. 1, doi: 10.1029/2004GC000841.

Maggi, A., and K. Priestley (2005). Surface waveform tomography of the Turkish-Iranian plateau, *Geophys. J. Int.* **160,** no. 3, 1068–1080.

Minson, S. E., M. Simons, and J. L. Beck (2013). Bayesian inversion for finite fault earthquake source models. I–Theory and algorithm, *Geophys. J. Int.* **194,** no. 3, 1701–1726.

Reilinger, R., S. McClusky, P. Vernant, S. Lawrence, S. Ergintav, R. Cakmak, H. Ozener, F. Kadirov, I. Guliev, R. Stepanyan, M. Nadariya, G. Hahubia, S. Mahmoud, K. Sakr, A. ArRajehi, D.

Paradissis, A. Al-Aydrus, M. Prilepin, T. Guseva, E. Evren, A. Dmitrotsa, S. V. Filikov, F. Gomez, R. Al-Ghazzi, and G. Karam (2006). GPS constraints on continental deformation in the Africa-Arabia-Eurasia continental collision zone and implications for the dynamics of plate interactions, *J. Geophys. Res.* **111,** no. B5, B05411, doi: 10.1029/2005JB004051.

Rosen, P. A., S. Hensley, I. R. Joughin, F. K. Li, S. N. Madsen, E. Rodriguez, and R. M. Goldstein (2000). Synthetic aperture radar interferometry, *Proc. IEEE* **88,** no. 3, 333–382.

Sambridge, M. (1999). Geophysical inversion with a neighbourhood algorithm-I. Searching a parameter space, *Geophys. J. Int.* **138,** no. 2, 479–494.

Satyabala, S. P., Z. Yang, and R. Bilham (2012). Stick-slip advance of the Kohat plateau in Pakistan, *Nat. Geosci.* **5,** no. 2, 147–150.

Simons, M., Y. Fialko, and L. Rivera (2002). Coseismic deformation from the 1999 M_w 7.1 Hector Mine, California, earthquake as inferred from InSAR and GPS observations, *Bull. Seismol. Soc. Am.* **92,** no. 4, 1390–1402.

Smith, G., L. McNeill, T. J. Henstock, and J. Bull (2012). The structure and fault activity of the Makran accretionary prism, *J. Geophys. Res.* **117,** no. B7, B07407, doi: 10.1029/2012JB009312.

Szeliga, W., R. Bilham, D. M. Kakar, and S. H. Lodi (2012). Interseismic strain accumulation along the western boundary of the Indian subcontinent, *J. Geophys. Res.* **117,** no. B8, B08404, doi: 10.1029/2011JB008822.

Ul-Hadi, S., S. D. Khan, L. A. Owen, A. S. Khan, K. A. Hedrick, and M. W. Caffee (2013). Slip-rates along the Chaman fault: Implication for transient strain accumulation and strain partitioning along the western Indian plate margin, *Tectonophysics* **608,** no. C, 389–400.

Wegmuller, U., and C. Werner (1997). Gamma SAR processor and interferometry software, in *Proc. of the Third ERS Symposium on Space at the Service of our Environment*, Florence, Italy.

Wesnousky, S. G. (2006). Predicting the endpoints of earthquake ruptures, *Nature* **444,** no. 7117, 358–360.

Zhu, L., and L. Rivera (2002). A note on the dynamic and static displacements from a point source in multilayered media, *Geophys. J. Int.* **148,** 619–627.

Seismological Laboratory
Department of Geological and Planetary Sciences
California Institute of Technology
1200 E California Blvd
Pasadena, California 91125
(R.J., Z.D., B.R., M.S., S.E.M., H.Z., M. A. G..A.)

Tectonics Observatory
Department of Geological and Planetary Sciences
California Institute of Technology
1200 E California Blvd
Pasadena, California 91125
(F.A., S.L.)

Institut de Physique du Globe de Strasbourg
UdS and EOST/CNRS UMR 7516
France
(L.R.)

Natural Resources Canada
560 Rochester Street
Ottawa, Ontario K1A 0Y7 Canada
(S.S.)

Department of Geodesy and Remote Sensing
Helmholtz Center Potsdam
GFZ, Telegrafenberg Haus A17
14473 Potsdam, Germany
(M.M.)

Jet Propulsion Laboratory
California Institute of Technology
Pasadena, California 91109
(E.J.F.)

Manuscript received 10 December 2013;
Published Online 25 March 2014